



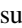



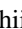
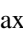







ALMA CO Observations of the Gamma-Ray Supernova Remnant RX J1713.7–3946: Discovery of Shocked Molecular Cloudlets and Filaments at 0.01 pc Scales

H. Sano^{1,2,3} , T. Inoue², K. Tokuda^{1,4} , T. Tanaka⁵ , R. Yamazaki^{6,7} , S. Inutsuka² , F. Aharonian^{8,9,10}, G. Rowell¹¹ , M. D. Filipović¹² , Y. Yamane² , S. Yoshiike² , N. Maxted¹³ , H. Uchida⁵ , T. Hayakawa² , K. Tachihara² , Y. Uchiyama¹⁴, and Y. Fukui^{2,3}

¹ National Astronomical Observatory of Japan, Mitaka, Tokyo 181-8588, Japan; hidetoshi.sano@nao.ac.jp

² Department of Physics, Nagoya University, Furo-cho, Chikusa-ku, Nagoya 464-8601, Japan

³ Institute for Advanced Research, Nagoya University, Furo-cho, Chikusa-ku, Nagoya 464-8601, Japan

⁴ Department of Physical Science, Graduate School of Science, Osaka Prefecture University, 1-1 Gakuen-cho, Naka-ku, Sakai 599-8531, Japan

⁵ Department of Physics, Kyoto University, Kitashirakawa Oiwake-cho, Sakyo, Kyoto 606-8502, Japan

⁶ Department of Physics and Mathematics, Aoyama Gakuin University, 5-10-1 Fuchinobe, Sagami-hara 252-5258, Japan

⁷ Institute of Laser Engineering, Osaka University, 2-6 Yamadaoka, Suita, Osaka 565-0871, Japan

⁸ Dublin Institute for Advanced Studies, 31 Fitzwilliam Place, Dublin 2, Ireland

⁹ Max-Planck-Institut für Kernphysik, P.O. Box 103980, D-69029 Heidelberg, Germany

¹⁰ Gran Sasso Science Institute, 7 viale Francesco Crispi, I-67100 L'Aquila, Italy

¹¹ School of Physical Sciences, The University of Adelaide, North Terrace, Adelaide, SA 5005, Australia

¹² Western Sydney University, Locked Bag 1797, Penrith South DC, NSW 1797, Australia

¹³ School of Science, University of New South Wales, Australian Defence Force Academy, Canberra, ACT 2600, Australia

¹⁴ Department of Physics, Rikkyo University, 3-34-1 Nishi Ikebukuro, Toshima-ku, Tokyo 171-8501, Japan

Received 2020 October 7; revised 2020 November 3; accepted 2020 November 5; published 2020 November 27

Abstract

RX J1713.7–3946 is a unique core-collapse supernova remnant (SNR) that emits bright TeV gamma-rays and synchrotron X-rays caused by cosmic rays, in addition to interactions with interstellar gas clouds. We report here on results of Atacama Large Millimeter/submillimeter Array ¹²CO($J = 1-0$) observations toward the northwestern shell of the SNR. We newly found three molecular complexes consisting of dozens of shocked molecular cloudlets and filaments with typical radii of $\sim 0.03-0.05$ pc and densities of $\sim 10^4$ cm⁻³. These cloudlets and filaments are located not only along synchrotron X-ray filaments, but also in the vicinity of X-ray hotspots with month- or year-scale time variations. We argue that X-ray hotspots and filaments were generated by shock–cloudlet interactions through magnetic-field amplification up to mG. The interstellar medium density contrast of $\sim 10^5$, coexistence of molecular cloudlets and low-density diffuse medium of ~ 0.1 cm⁻³, is consistent with such a magnetic field amplification as well as a wind-bubble scenario. The small-scale cloud structures also affect hadronic gamma-ray spectra considering the magnetic field amplification on surface and inside clouds.

Unified Astronomy Thesaurus concepts: Supernova remnants (1667); Interstellar medium (847); Cosmic ray sources (328); Gamma-ray sources (633); X-ray sources (1822)

1. Introduction

Galactic cosmic rays are believed to be accelerated by shockwaves in supernova remnants (SNRs) via the diffusive shock acceleration (DSA; Bell 1978; Blandford & Ostriker 1978), and cosmic-ray induced nonthermal radiation has been predicted and/or detected from various SNRs (e.g., Aharonian et al. 1994; Drury et al. 1994). In general, the classical DSA theory assumes uniform density distribution of the interstellar medium (ISM) surrounding SNRs. However, observational results indicated that nonthermal X-ray and/or gamma-ray bright SNRs are tightly interacting with dense and clumpy gaseous medium such as molecular and atomic clouds (e.g., Fukui et al. 2003, 2017; Aharonian et al. 2008; Zhou et al. 2016; Sano et al. 2020). A key issue at present is how shock–cloud interaction affects radiation processes of the nonthermal radiation, as well as acceleration mechanisms of cosmic rays beyond the DSA.

The core-collapse SNR RX J1713.7–3946 (a.k.a. G347.3–0.5) provides the best laboratory to test the effect because of its bright nonthermal X-rays and TeV gamma-rays (e.g., Koyama et al. 1997; Aharonian et al. 2004), in addition to certain interactions with dense gas clouds at the close distance of 1 kpc (e.g., Fukui et al. 2003; Moriguchi et al. 2005; Sano et al. 2010;

Maxted et al. 2012) and its young age of ~ 1600 yr (Wang et al. 1997; Fukui et al. 2003; Tsuji & Uchiyama 2016). The X-rays are dominated by synchrotron radiation up to 120 keV (e.g., Slane et al. 1999; Tanaka et al. 2008; Tsuji et al. 2019; Kuznetsova et al. 2019). Chandra observations discovered year-scale time variability of X-ray hotspots on the order of 10 arcsec or 0.05 pc widths as well as X-ray filaments of $\sim 0.1-0.2$ pc widths, indicating efficient cosmic-ray acceleration with amplified magnetic field (Uchiyama et al. 2007; Higurashi et al. 2020). The TeV gamma-ray observations of RX J1713.7–3946 revealed its shell-like morphology with photon energies from 200 GeV to 40 TeV (Aharonian et al. 2004, 2006, 2007; H.E.S.S. Collaboration et al. 2018). Despite a number of efforts to model the broadband spectra, the origin of gamma-rays—hadronic, leptonic, or a combination of both—was not clearly established because all scenarios could reproduce the observed spectra (see H.E.S.S. Collaboration et al. 2018 and references therein).

Investigating the interstellar gas associated with RX J1713.7–3946 holds a key to understanding the radiation processes and efficient acceleration of cosmic rays. Fukui et al. (2012) presented a good spatial correspondence between the TeV gamma-rays and ISM proton column density. This provides an essential condition for gamma-rays to be predominantly of

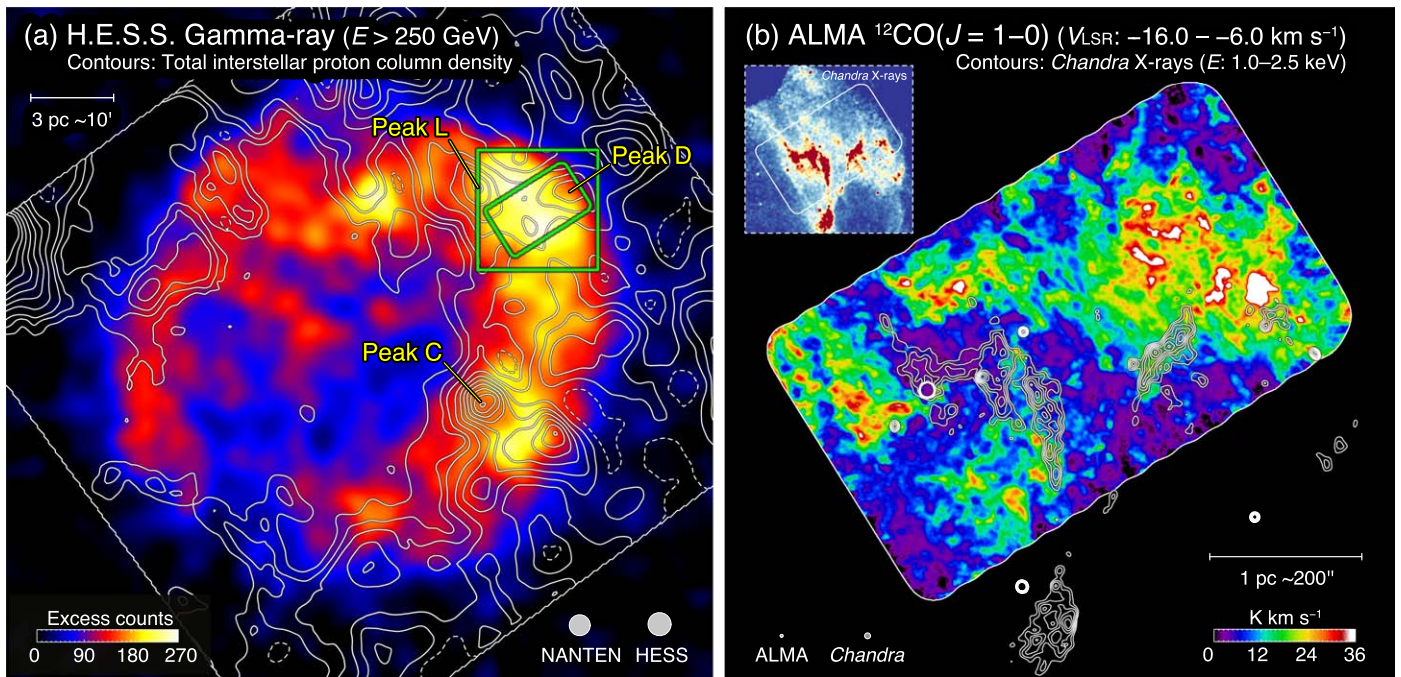


Figure 1. (a) TeV gamma-ray excess map of RX J1713.7–3946 in equatorial coordinates obtained by H.E.S.S. (H.E.S.S. Collaboration et al. 2018). Superposed contours indicate the ISM proton column density (Fukui et al. 2012). The contour levels are 6, 7, 8, 10, 12, 14, 16, 18, 20, and $22 \times 10^{21} \text{ cm}^{-2}$. Green rectangles represent the ALMA observed area (small rectangle) and to be presented area in Figure 1(b). (b) ALMA CO map toward the northwest of RX J1713.7–3946. Superposed contours indicate the X-ray intensity obtained with Chandra (Uchiyama et al. 2007). The lowest contour and contour intervals are 9.5×10^{-8} and 9.5×10^{-9} photons $\text{cm}^{-2} \text{ s}^{-1} \text{ pixel}^{-1}$, respectively. The colored image in the top left indicates Chandra X-ray map in the same region as shown in Figure 1(b).

hadronic origin. Sano et al. (2010, 2013) found limb-brightening of synchrotron X-rays toward shocked molecular clouds with a size of ~ 3 pc, where the small photon indices of synchrotron X-rays are seen (Sano et al. 2015; Okuno et al. 2018). The authors proposed a possible scenario that the shock–cloud interaction generates turbulence that enhances magnetic field and synchrotron X-rays on the surface of shocked clouds. Moreover, the enhanced turbulence and/or magnetic field may re-accelerate electrons into higher energy. This interpretation is also supported by numerical results, and well explains the observed broadband spectra without bright thermal X-rays (e.g., Inoue et al. 2009, 2012; Celli et al. 2019). However, previous studies could not spatially resolve tiny molecular clouds relating to the X-ray hotspots and filaments at 0.05 pc scales that were predicted by Inoue et al. (2009).

We report here on results of Atacama Large Millimeter/submillimeter Array (ALMA) CO observations toward the northwestern shell of RX J1713.7–3946 with a spatial resolution of ~ 0.02 pc. Our findings for complexes of molecular cloudlets at 0.01 pc provide a new perspective on the ISM surrounding core-collapse SNRs.

2. Results

Figure 1(a) shows the overall TeV gamma-ray morphology of RX J1713.7–3946 (H.E.S.S. Collaboration et al. 2018). The TeV gamma-ray shell shows a good spatial correspondence with the total interstellar proton column density contours (Fukui et al. 2012). For the dense star-forming core named “peak C,” TeV gamma-ray intensity is reduced respect to its surroundings. Note that the brightest TeV gamma-ray spot is located in the northwestern shell, especially in the intermediate

region of peaks D and L. The intercloud region also bright in X-rays with filamentary structures.

Figure 1(b) shows the $^{12}\text{CO}(J = 1-0)$ integrated intensity map obtained using ALMA (see Appendix A.1 for detailed information of observations and data reduction). The integration range of -16 – -6 km s^{-1} is typical radial velocity in the northwestern molecular clouds, which is certainly associated with RX J1713.7–3946 (e.g., Fukui et al. 2003, 2012; Moriguchi et al. 2005; Sano et al. 2010, 2013, 2015; Maxted et al. 2012). We newly identified three molecular complexes with a size of ~ 1 pc toward the southeastern half of the ALMA observed area, in addition to the previously known molecular cloud peak D. The X-ray bright filaments as shown by contours are nicely along not only with the three molecular complexes (hereafter RXJ1713NW-East), but also with a part of the molecular cloud peak D (hereafter RXJ1713NW-West). It is noteworthy that intercloud diffuse regions show significantly low intensity (purple colored areas), whereas there are several tiny CO clumps with a size on the order of 0.01 pc. We hereafter refer to the tiny CO clumps as “molecular cloudlets.”

Figures 2(a)–2(c) show the velocity channel maps of ALMA CO toward RXJ1713NW-East. We confirmed that one of the newly identified molecular complexes consists of dozens of molecular cloudlets (e.g., CL1–6) and filaments (e.g., Figure 2(b), ~ 0.06 pc width). Almost all of the molecular cloudlets and filaments are spatially associated with the X-ray filaments, but the X-ray minor peaks and X-ray hotspots identified by Higurashi et al. (2020) are located in the intercloud regions. The typical spatial separations between X-ray minor peaks or hotspots and nearest CO intensity peaks are ~ 0.05 – 0.15 pc. The bottom row of Figure 2 shows CO line profiles of the typical molecular cloudlets CL1–6, which are located near the X-ray filaments and hotspots without contamination. All of the sampled molecular cloudlets are

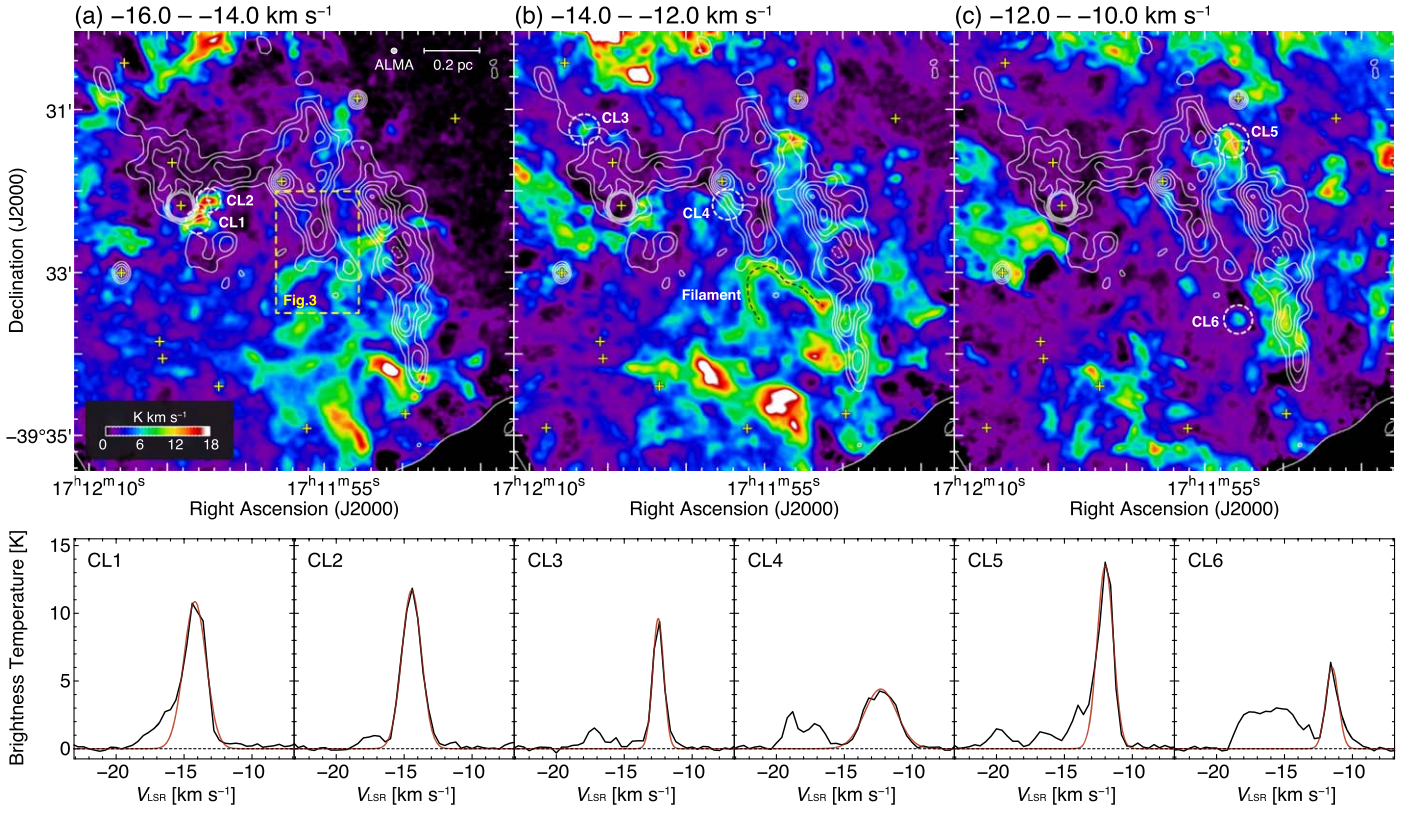


Figure 2. Top row: ALMA CO velocity channel maps toward RXJ1713NW-East. Each panel shows CO intensity distribution integrated every 2.0 km s^{-1} in the velocity range from -16.0 to -10.0 km s^{-1} . Superposed contours indicate the same X-ray intensity as shown in Figure 1(b). Yellow crosses indicate positions of X-ray hotspots identified by Higurashi et al. (2020). The typical CO cloudlets, CL1–6, and a CO filament are also indicated. Bottom row: ALMA CO profiles of CL1–6 (black solid lines). Each spectrum is fitted by a single Gaussian kernel using the least-squares method.

Table 1
Physical Properties of Typical CO Cloudlets Associated with RX J1713.7–3946

Name	α_{J2000} (h m s)	δ_{J2000} ($^{\circ}$ ' ")	T_{mb} (K)	V_{peak} (km s^{-1})	ΔV (km s^{-1})	Size (pc)	Mass (M_{\odot})	$n(\text{H}_2)$ (cm^{-3})
(1)	(2)	(3)	(4)	(5)	(6)	(7)	(8)	(9)
CL1	17 12 02.95	−39 32 20.4	10.9 ± 0.6	-14.20 ± 0.05	1.94 ± 0.14	0.08	0.37	2.6×10^4
CL2	17 12 02.50	−39 32 06.7	11.7 ± 0.2	-14.45 ± 0.01	1.70 ± 0.03	0.07	0.27	3.1×10^4
CL3	17 12 06.48	−39 31 14.7	9.6 ± 0.4	-12.50 ± 0.02	0.95 ± 0.04	0.06	0.08	1.6×10^4
CL4	17 11 57.33	−39 32 08.1	4.4 ± 0.2	-12.32 ± 0.05	2.79 ± 0.12	0.10	0.33	1.2×10^4
CL5	17 11 53.17	−39 31 21.3	13.5 ± 0.9	-11.99 ± 0.05	1.38 ± 0.11	0.10	0.47	2.0×10^4
CL6	17 11 52.72	−39 33 35.2	6.0 ± 0.6	-11.49 ± 0.06	1.09 ± 0.14	0.07	0.08	1.0×10^4

Note. Col. (1): cloudlet name. Cols. (2–9): observed properties of cloudlets obtained by single Gaussian fitting with $^{12}\text{CO}(J=1-0)$ emission line. Cols. (2)–(3): position of cloudlets. Col. (4): maximum brightness temperature. Col. (5): central velocity. Col. (6): FWHM linewidth. Col. (7): effective diameter of cloudlets defined as $(S/\pi)^{0.5} \times 2$, where S is the surface area of cloudlets surrounded by a contour of the half level of maximum integrated intensity. Col. (8): mass of cloudlets defined as $m_{\text{p}}\mu\Omega D^2 \sum_i [N_i(\text{H}_2)]$, where m_{p} is the atomic hydrogen mass, μ is the mean molecular weight, D is the distance to the SNR, Ω is the solid angle in a spatial pixel, and $N(\text{H}_2)$ is molecular hydrogen column density for each pixel. We used $\mu = 2.8$ and an equation of $N(\text{H}_2)/W(\text{CO}) = 2.0 \times 10^{20} (\text{K km s}^{-1})^{-1} \text{ cm}^{-2}$, where $W(\text{CO})$ is the CO integrated intensity (Bertsch et al. 1993). Col. (9): number density of molecular hydrogen $n(\text{H}_2)$.

significantly detected, and show the narrow velocity width ($<2 \text{ km s}^{-1}$) except for CL4. Although wing-like profiles are seen toward CL1 and CL5, these can be explained by other overlapped molecular cloudlets. The physical properties of molecular cloudlets CL1–6 are summarized in Table 1. The typical diameters and masses of molecular cloudlets are ~ 0.06 – 0.10 pc and ~ 0.1 – $0.5 M_{\odot}$, respectively. The number densities of molecular cloudlets are a few 10^4 cm^{-3} , which were obtained using a CO-to- H_2 conversion factor (see the note in Table 1).

Figure 3 shows the enlarged view of the X-ray filament from which flux time variability was reported by Uchiyama et al. (2007). We compared spatial distributions of CO and X-rays for each observing epoch (see Appendix A.2 for details). Two X-ray hotspots in 2000 July (Figure 3(b)) and 2009 May (Figure 3(f)) are significantly detected. The former was previously reported by Uchiyama et al. (2007), whereas the latter is newly identified ($\sim 4\sigma$ above the surrounding level). The latter hotspot was excited within three years and

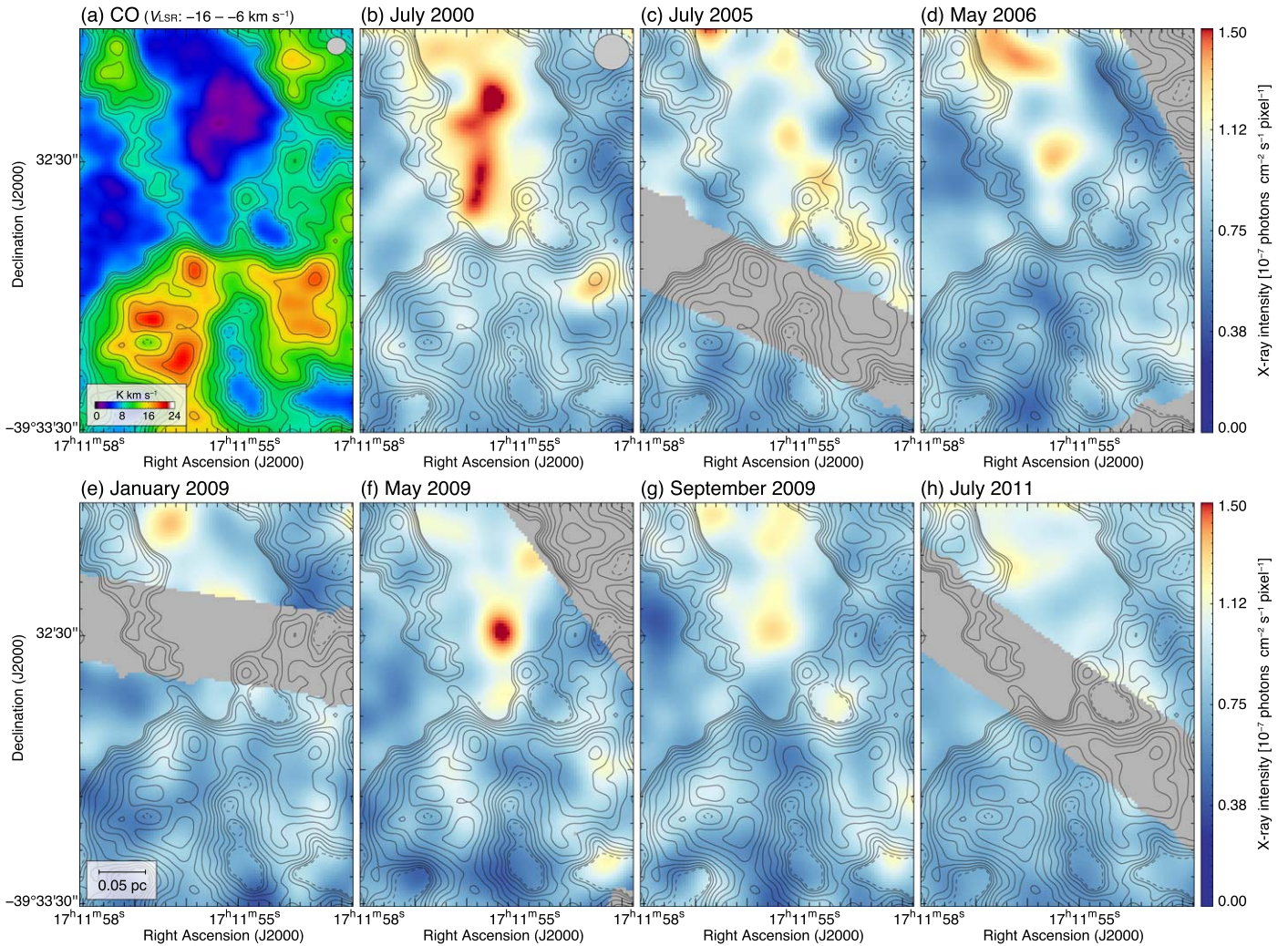


Figure 3. (a) Enlarged view of ALMA CO map toward an X-ray hotspot presented by Uchiyama et al. (2007). (b–h) Sequence of X-ray observations in 2000 July, 2005 July, 2006 May, 2009 January, 2009 May, 2009 September, and 2011 July. All X-ray images show the same intensity scales. Superposed contours indicate the CO intensity. Gray shaded areas were eliminated due to low exposure time (see the text).

disappeared within four months. It should be also noted that these hotspots are located on the intercloud or low-density region, but not in the direction of dense cloudlets.

3. Discussion

3.1. Origin of Highly Inhomogeneous Density Distribution

We spatially resolved shocked molecular cloudlets and filaments toward the northwestern shell of RX J1713.7–3946. These clumpy structures at 0.01 pc scales coexist with the low-density intercloud medium. We argue that the highly inhomogeneous gas environment provides conclusive evidence for a wind-bubble scenario proposed by Fukui et al. (2012) and Inoue et al. (2012). Before the supernova explosion, the high-mass progenitor of RX J1713.7–3946 ejected its outer hydrogen layer as stellar winds over a timescale of several 10^6 years. The pre-existent intercloud diffuse gas was completely swept up and a low-density wind bubble with a density of $\sim 0.01\text{--}0.1 \text{ cm}^{-3}$ was created (e.g., Weaver et al. 1977). On the other hand, molecular cloudlets and filaments can survive wind erosion due to their high density $\sim 10^4 \text{ cm}^{-3}$. Moreover, according to synthetic observations of magneto-hydrodynamic (MHD) simulation for colliding HI clouds,

~ 0.1 pc clouds could be newly formed by stellar wind compression (e.g., Fukui et al. 2018; Tachihara et al. 2021). After the passage of the supernova shock wave, dense cloudlets and filaments will not be deformed or evaporated owing to short interacting time. In fact, numerical simulations show that a molecular cloud with the size 0.2 pc and density 10^3 cm^{-3} can survive shock erosion at least 300 years after the passage of shocks (Celli et al. 2019). The CO line emission without line-broadening or wing-like profiles also supports this idea.

Note that such inhomogeneous gas density distribution is also expected in other core-collapse SNRs. Further ALMA observations with high special resolution on the order of 0.01 pc are needed for complete understanding the interstellar environment surrounding the SNRs.

3.2. Magnetic Field Amplification via Shock–Cloudlet Interactions

Uchiyama et al. (2007) discovered X-ray hotspots in the northwestern shell of RX J1713.7–3946, which show year-scale time variability of X-ray flux with the typical spatial scale of ~ 0.05 pc. Considering the acceleration and radiative cooling time of cosmic-ray electrons, the authors concluded that the time variability was caused by amplified magnetic field of mG.

Most recently, Higurashi et al. (2020) presented a detailed analysis of 65 X-ray hotspots; about one-third of them showed year-scale time variabilities and eight hotspots showed monthly variabilities with significance of at least 3σ . The authors proposed that the time variabilities are caused by dense cloud cores with a density of 10^5 – 10^7 cm^{-3} . In the present section, we argue that the observed time variabilities can be understood by the magnetic field amplification through interactions between shockwaves and cloudlets with a density of $\sim 10^4$ cm^{-3} .

We estimate the magnetic field strength toward the newly identified X-ray hotspot, following the method by Uchiyama et al. (2007) and Higurashi et al. (2020). The radiative cooling time of electrons T_{synch} can be written as

$$T_{\text{synch}} \sim 1.5 \left(\frac{B}{1 \text{ mG}} \right)^{-1.5} \left(\frac{\varepsilon}{1 \text{ keV}} \right)^{-0.5} \text{ (yr)} \quad (1)$$

where ε is the photon energy of synchrotron X-rays and B is the magnetic field strength. Considering the short decay time of four months and $\varepsilon = 1$ keV, we can obtain ~ 3 mG toward the X-ray hotspot. On the other hand, the acceleration time of electrons T_{acc} can be expressed in terms of gyro-factor $\eta = (B/\delta B)^2$ and shock velocity V_s as

$$T_{\text{acc}} \sim 1\eta \left(\frac{B}{1 \text{ mG}} \right)^{-1.5} \left(\frac{\varepsilon}{1 \text{ keV}} \right)^{0.5} \left(\frac{V_s}{3000 \text{ km s}^{-1}} \right)^{-2} \text{ (yr)}. \quad (2)$$

Adopting observed values of $\eta = 1$ (Tsuji et al. 2019) and $V_s = 3900$ km s^{-1} (Tsuji & Uchiyama 2016), the magnetic field strength B is estimated to ~ 300 μG . Note that it is natural to have different magnetic field in Equations (1) and (2), because cosmic rays do not need to be accelerated in the same location.

We argue that the strong magnetic field in X-ray hotspots as well as diffuse X-ray filaments was generated by shock–cloudlet interactions. According to MHD simulations by Inoue et al. (2009, 2012), the shock–cloud interaction generates multiple eddies that enhance magnetic field strength up to mG on the surface of dense HI clouds with a density of $\sim 10^2$ cm^{-3} . Subsequent numerical simulation confirmed that the magnetic field is also amplified by interactions between shocks and a molecular clump with a density of 10^3 cm^{-3} (Celli et al. 2019). Note that the most enhanced magnetic field is placed ~ 0.4 pc away from the shocked cloud by adopting the cloud size of 0.2 pc and the ISM density contrast of $\sim 10^5$ (see Figure 3 in Celli et al. 2019). For the northwestern shell of RX J1713.7–3946, the ISM density contrast is estimated to $\sim 10^5$ considering the electron density in an intercloud region ~ 0.10 – 0.13 cm^{-3} (Katsuda et al. 2015) and the cloudlet density $\sim 10^4$ cm^{-3} . Therefore, the highest magnetic field is expected to be ~ 0.12 – 0.20 pc away from the observed cloudlet with sizes of 0.06–0.10 pc, which is roughly consistent with observed separations between the X-ray hotspots/filaments and cloudlets.¹⁵

¹⁵ Actual spatial separation between cloudlet and the highest magnetic field will be slightly modified considering the shape of shocked cloudlet and projected distance. For the case of Figure 3, we assumed the cylinder shape of shocked cloud as an extension of spherical cloud assumed by Celli et al. (2019).

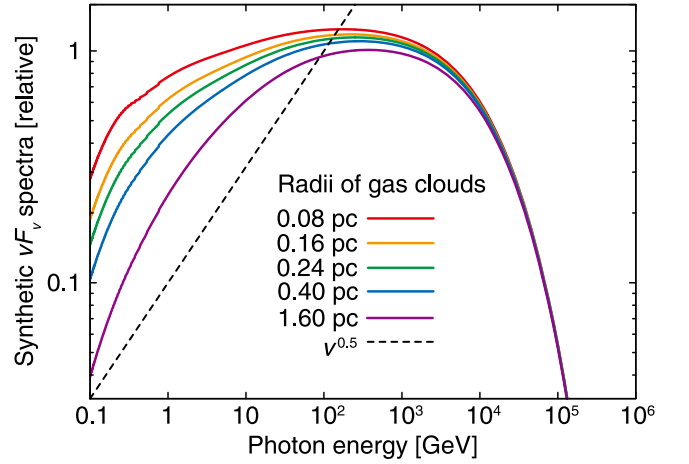


Figure 4. Synthetic νF_ν gamma-ray spectra expected from shocked gas clouds with radii of 0.08, 0.16, 0.24, 0.40, and 1.60 pc, which were reproduced using numerical results in Inoue (2019). The dashed line indicates $\nu F_\nu \propto \nu^{0.5}$.

The shock–cloudlet interaction may also induce the spectrum modulation of synchrotron X-rays. Previous observational studies also indicate spectral flattening toward the shock interacting region (e.g., Sano et al. 2015; Okuno et al. 2018; Tanaka et al. 2020). Further spatially resolved X-ray spectroscopy based on distributions of molecular clouds reveals such spectrum modulations.

3.3. Prospects for Gamma-Ray Spectra toward the Northwestern Shell

It is thought that the hadronic gamma-ray shows flat νF_ν spectrum from the pion-creation threshold energy at ~ 0.1 GeV to the maximum energy achieved by DSA, whereas the leptonic gamma-ray shows hard νF_ν spectrum instead. Because the Fermi-LAT detected the hard spectrum with photon index of 1.5, this was often used to reject the hadronic gamma-ray scenario from RX J1713.7–3946 (e.g., Abdo et al. 2011). On the other hand, the hadronic gamma-ray can be harder spectrum by considering the inhomogeneous gas distribution and energy-dependent diffusion of cosmic-ray protons (e.g., Gabici et al. 2009; Zirakashvili & Aharonian 2010; Inoue et al. 2012; Gabici & Aharonian 2014). In this section, we argue that the hadronic gamma-ray spectrum from the northwestern shell of RX J1713.7–3946 will possibly be flatter than spatially combined spectra.

According to Inoue et al. (2012), the penetration depth of a relativistic particle into molecular clouds l_{pd} can be described as

$$l_{\text{pd}} = 0.1 \eta^{0.5} \left(\frac{E}{10 \text{ TeV}} \right)^{0.5} \left(\frac{B}{100 \mu\text{G}} \right)^{-0.5} \left(\frac{t}{1000 \text{ yr}} \right)^{0.5} \text{ (pc)}, \quad (3)$$

where E is the particle energy and t is the elapsed time passed since the forward shock encountered the molecular cloud. The magnetic field will be enhanced not only on the surface of shocked clouds via shock interaction, but also inside the clouds caused by cosmic-ray streaming what is called Bell instability (Bell 2004). Inoue (2019) argued that the Bell instability induced magnetic field amplification prevent further cosmic-ray penetration into shocked clouds by diminishing the diffusion

coefficient for the cosmic-ray energy below ~ 1 TeV. Note that the degree of magnetic field amplification depends on path length from the surface of shocked clouds, roughly corresponding to a radius of shocked clouds.

Figure 4 shows νF_ν spectra of hadronic gamma-rays with various cloud radii. According to Moriguchi et al. (2005), typical radii of molecular clouds associated with the SNR were derived as ~ 1 – 2 pc. The densest star-forming cloud peak C in the southwestern shell is a typical example with a featureless morphology and central concentration density gradient with an outer radius of ~ 1.5 pc (Sano et al. 2010). Therefore, it is natural to be observed hard gamma-ray spectra ($\nu^{0.5}$ or photon index of 1.5) when we combined them for the entire remnant (e.g., Abdo et al. 2011). On the other hand, the brightest gamma-ray peak in the northwestern shell is associated with dozens of molecular cloudlets and filaments with typical radii of 0.03–0.05 pc, suggesting that the flatter gamma-ray spectrum will be expected than the case of 0.08 pc in red curve of Figure 4. Future detailed spatially resolved spectroscopy of gamma-rays using the Cherenkov Telescope Array (CTA) has a potential to resolve such spatial difference of gamma-ray spectral shape.

In case we do not detect the gamma-ray spectrum flattening in the northwestern shell of RX J1713.7–3946 using CTA, it can be explained that the magnetic field in the cloudlet surface is more efficiently enhanced than inside the cloud via the shock–cloudlet interaction. This is because a smaller cloud size induces a shorter timescale of magnetic field amplification, even if the maximum magnetic field strength does not depend on the cloud size. Alternatively, the diffusion length of cosmic rays could be shorter than 0.1 pc if the actual elapsed time in Equation (3) is significantly smaller than 1000 yr. In fact, CO cloudlets in RXJ1713NW-East have been fully overtaken by the shocks, while the peak D including RXJ1713NW-West is likely now interacting with the forward shock (e.g., Sano et al. 2013). In any case, the clumpy cloud distribution interacting with shockwaves is important in understanding the gamma-ray and X-ray spectra from shock-accelerated cosmic rays in SNRs.

4. Summary

By using ALMA, we have spatially resolved molecular complexes consisting of the 0.01 pc scale cloudlets and filaments interacting with the northwestern shell of RX J1713.7–3946, where the brightest TeV gamma-rays and synchrotron X-ray filaments/hotspots are detected. The molecular cloudlets have a typical radii of ~ 0.03 – 0.05 pc and densities of $\sim 10^4$ cm $^{-3}$ along with X-ray filaments and hotspots, indicating that magnetic field is amplified through shock–cloudlet interactions. The ISM density contrast is to be $\sim 10^5$, consistent with a wind-bubble scenario. The small-scale structures or density fluctuations of the ISM may induce spectral modulations for both the hadronic gamma-rays and synchrotron X-rays, beyond the standard DSA.

This Letter makes use of the following ALMA data: ADS/JAO.ALMA#2017.1.01406.S. ALMA is a partnership of ESO (representing its member states), NSF (USA) and NINS (Japan), together with NRC (Canada), MOST and ASIAA (Taiwan), and KASI (Republic of Korea), in cooperation with the Republic of Chile. The Joint ALMA Observatory is operated by ESO, AUI/NRAO, and NAOJ. This study was

supported by JSPS KAKENHI grant Nos. JP18H01232 (R.Y.), JP19K14758 (H.S.), and JP19H05075 (H.S.). K. Tokuda was supported by NAOJ ALMA Scientific Research grant No. of 2016-03B. We appreciate the anonymous referee for useful comments and suggestions, which helped authors to improve the paper.

Appendix A Observations and Data Reductions

A.1. ALMA CO


Observations of $^{12}\text{CO}(J=1-0)$ line emission at 115 GHz were carried out using the ALMA Band 3 (86–116 GHz) during Cycle 5 (PI: H. Sano, proposal ID 2017.1.01406.S). We used 46 antennas of 12-m array, 12 antennas of 7-m array, and four antennas of total power (TP) array. The observed area was $11'1 \times 6'4$ rectangular region centered at $(\alpha_{J2000}, \delta_{J2000}) = (17^{\text{h}}11^{\text{m}}48^{\text{s}}0, -39^{\circ}30'57''.6)$. The combined baseline length of 12-m and 7-m arrays is from 8.9 to 313.7 m, corresponding to u – v distances from 3.4 to 120.6 $k\lambda$. The data were processed using the Common Astronomy Software Application (CASA; McMullin et al. 2007) package version 5.6.0. We utilized the “tclean” task with natural weighting and “multi-scale” deconvolution algorithm implemented in the CASA package (Cornwell 2008). We applied “uvtaper” during the clean processes to improve the imaging quality. We combined the cleaned interferometer data (12-m+7-m) and calibrated TP array data by using “feather” task. The beam size of feathered image is $4''.37 \times 3''.89$ with a position angle of $-86^\circ 6'$, corresponding to a spatial resolution of ~ 0.02 pc at the distance of 1 kpc. The typical noise fluctuations of the feathered image are ~ 0.13 K at a velocity resolution of 0.4 km s $^{-1}$.

A.2. Chandra X-Rays

We utilized archival X-ray data obtained using Chandra, for which the observation IDs are 736, 5560, 6370, 10090, 10091, 10092, and 12671 (PI: P. Slane for 736 and Y. Uchiyama for the others), which were published in previous papers (Lazendic et al. 2003, 2004; Uchiyama et al. 2003, 2007; Tsuji & Uchiyama 2016; Okuno et al. 2018; Tsuji et al. 2019; Higurashi et al. 2020). The X-ray data were taken with the Advanced charge-coupled device Imaging Spectrometer I-array on July 2000, July 2005, May 2006, January/May/September 2009, and July 2011. We used Chandra Interactive Analysis of Observations (CIAO; Fruscione et al. 2006) software version 4.12 with CALDB 4.9.1 for data reprocessing and imaging. All the downloaded data were reprocessed using the “chandra_repro” task. We then created energy-filtered, exposure-corrected images using the “fluximage” task for each observation, where the energy band of 1–2.5 keV. To eliminate regions with low photon statistics, we also masked areas with 60% or less of maximum exposure time for each observation.

ORCID iDs

H. Sano  <https://orcid.org/0000-0003-2062-5692>
 K. Tokuda  <https://orcid.org/0000-0002-2062-1600>
 T. Tanaka  <https://orcid.org/0000-0002-4383-0368>
 R. Yamazaki  <https://orcid.org/0000-0002-1251-7889>
 S. Inutsuka  <https://orcid.org/0000-0003-4366-6518>
 G. Rowell  <https://orcid.org/0000-0002-9516-1581>

M. D. Filipović  <https://orcid.org/0000-0002-4990-9288>
 Y. Yamane  <https://orcid.org/0000-0001-8296-7482>
 S. Yoshiike  <https://orcid.org/0000-0002-2458-7876>
 N. Maxted  <https://orcid.org/0000-0003-2762-8378>
 H. Uchida  <https://orcid.org/0000-0003-1518-2188>
 T. Hayakawa  <https://orcid.org/0000-0003-0324-1689>
 K. Tachihara  <https://orcid.org/0000-0002-1411-5410>

References

- Abdo, A. A., Ackermann, M., Ajello, M., et al. 2011, *ApJ*, 734, 28
 Aharonian, F., Akhperjanian, A. G., Bazer-Bachi, A. R., et al. 2006, *A&A*, 449, 223
 Aharonian, F., Akhperjanian, A. G., Bazer-Bachi, A. R., et al. 2007, *A&A*, 464, 235
 Aharonian, F., Akhperjanian, A. G., Bazer-Bachi, A. R., et al. 2008, *A&A*, 481, 401
 Aharonian, F. A., Akhperjanian, A. G., Aye, K.-M., et al. 2004, *Natur*, 432, 75
 Aharonian, F. A., Drury, L. O., & Voelk, H. J. 1994, *A&A*, 285, 645
 Bell, A. R. 1978, *MNRAS*, 182, 147
 Bell, A. R. 2004, *MNRAS*, 353, 550
 Bertsch, D. L., Dame, T. M., Fichtel, C. E., et al. 1993, *ApJ*, 416, 587
 Blandford, R. D., & Ostriker, J. P. 1978, *ApJL*, 221, L29
 Celli, S., Morlino, G., Gabici, S., et al. 2019, *MNRAS*, 487, 3199
 Cornwell, T. J. 2008, *ISTSP*, 2, 793
 Drury, L. O., Aharonian, F. A., & Voelk, H. J. 1994, *A&A*, 287, 959
 Fruscione, A., McDowell, J. C., Allen, G. E., et al. 2006, *Proc. SPIE*, 6270, 62701V
 Fukui, Y., Hayakawa, T., Inoue, T., et al. 2018, *ApJ*, 860, 33
 Fukui, Y., Moriguchi, Y., Tamura, K., et al. 2003, *PASJ*, 55, L61
 Fukui, Y., Sano, H., Sato, J., et al. 2012, *ApJ*, 746, 82
 Fukui, Y., Sano, H., Sato, J., et al. 2017, *ApJ*, 850, 71
 Gabici, S., & Aharonian, F. A. 2014, *MNRAS*, 445, L70
 Gabici, S., Aharonian, F. A., & Casanova, S. 2009, *MNRAS*, 396, 1629
 H.E.S.S. Collaboration, Abdalla, H., Abramowski, A., et al. 2018, *A&A*, 612, A6
 Higurashi, R., Tsuji, N., & Uchiyama, Y. 2020, *ApJ*, 899, 102
 Inoue, T. 2019, *ApJ*, 872, 46
 Inoue, T., Yamazaki, R., & Inutsuka, S.-I. 2009, *ApJ*, 695, 825
 Inoue, T., Yamazaki, R., Inutsuka, S.-I., et al. 2012, *ApJ*, 744, 71
 Katsuda, S., Acero, F., Tominaga, N., et al. 2015, *ApJ*, 814, 29
 Koyama, K., Kinugasa, K., Matsuzaki, K., et al. 1997, *PASJ*, 49, L7
 Kuznetsova, E., Krivonos, R., Churazov, E., et al. 2019, *MNRAS*, 489, 1828
 Lazentic, J. S., Slane, P. O., Gaensler, B. M., et al. 2003, *ApJL*, 593, L27
 Lazentic, J. S., Slane, P. O., Gaensler, B. M., et al. 2004, *ApJ*, 602, 271
 Maxted, N. I., Rowell, G. P., Dawson, B. R., et al. 2012, *MNRAS*, 422, 2230
 McMullin, J. P., Waters, B., Schiebel, D., et al. 2007, *adass XVI*, 376, 127
 Moriguchi, Y., Tamura, K., Tawara, Y., et al. 2005, *ApJ*, 631, 947
 Okuno, T., Tanaka, T., Uchida, H., et al. 2018, *PASJ*, 70, 77
 Sano, H., Fukuda, T., Yoshiike, S., et al. 2015, *ApJ*, 799, 175
 Sano, H., Plucinsky, P. P., Bamba, A., et al. 2020, *ApJ*, 902, 53
 Sano, H., Sato, J., Horachi, H., et al. 2010, *ApJ*, 724, 59
 Sano, H., Tanaka, T., Torii, K., et al. 2013, *ApJ*, 778, 59
 Slane, P., Gaensler, B. M., Dame, T. M., et al. 1999, *ApJ*, 525, 357
 Tachihara, K., Fukui, Y., Hayakawa, T., et al. 2021, *PASJ Under Review*, arXiv:1811.02224
 Tanaka, T., Uchida, H., Sano, H., et al. 2020, *ApJL*, 900, L5
 Tanaka, T., Uchiyama, Y., Aharonian, F. A., et al. 2008, *ApJ*, 685, 988
 Tsuji, N., & Uchiyama, Y. 2016, *PASJ*, 68, 108
 Tsuji, N., Uchiyama, Y., Aharonian, F., et al. 2019, *ApJ*, 877, 96
 Uchiyama, Y., Aharonian, F. A., & Takahashi, T. 2003, *A&A*, 400, 567
 Uchiyama, Y., Aharonian, F. A., Tanaka, T., et al. 2007, *Natur*, 449, 576
 Wang, Z. R., Qu, Q.-Y., & Chen, Y. 1997, *A&A*, 318, L59
 Weaver, R., McCray, R., Castor, J., et al. 1977, *ApJ*, 218, 377
 Zhou, P., Chen, Y., Zhang, Z.-Y., et al. 2016, *ApJ*, 826, 34
 Zirakashvili, V. N., & Aharonian, F. A. 2010, *ApJ*, 708, 965